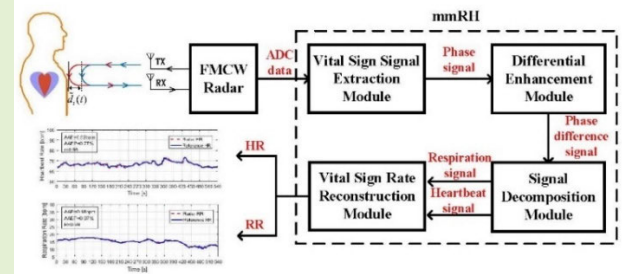


mmRH: Noncontact Vital Sign Detection With an FMCW mm-Wave Radar

Luyao Liu^{ID}, Jie Zhang^{ID}, *Member, IEEE*, Ying Qu^{ID}, Sen Zhang^{ID},
and Wendong Xiao^{ID}, *Senior Member, IEEE*

Abstract—Vital signs, such as respiration rate (RR) and heart rate (HR), are essential for human health status assessment. The radar could detect RR and HR in a noncontact manner by sensing the repetitive chest wall movement caused by cardiopulmonary activity, which is attractive due to the more comfortable experience and better privacy protection. However, as the chest wall displacement caused by heartbeat is much smaller than that caused by respiration, the weak heartbeat component may be easily overwhelmed by respiration harmonics, noise, and clutter, making it difficult to achieve accurate and reliable HR detection. In order to tackle this challenge, in this article, we design mmRH, a system that can accurately estimate RR as well as HR using a frequency-modulated continuous-wave (FMCW) millimeter-wave (mm-wave) radar, which consists of four functional modules. In the vital sign signal extraction module, the range bin corresponding to the body part with strong vital signs is determined to extract the vital sign signal, eliminating the clutter interference. The differential enhancement module is proposed to enhance the heartbeat component by the first-order temporal difference, reducing the impacts of respiration harmonics and noise on HR estimation. In the signal decomposition module, the respiration and heartbeat signals are separated via wavelet packet decomposition (WPD) to further suppress respiration harmonics and high-frequency noise of the heartbeat signal. In the vital sign rate reconstruction module, the sparse spectrum reconstruction (SSR) of vital sign rates is mapped to an adaptive filter and zero attracting sign exponentially forgetting least mean square (ZA-SEFLMS) algorithm is proposed to achieve high-resolution sparse spectrum for accurate and reliable RR and HR estimation. The effects of different settings, including the distance between the human subject and the radar, the sensor position, and the user heterogeneity, are investigated by extensive experiments. The results indicate that the designed mmRH could effectively suppress the respiration harmonics, noise, and clutter interference, and bring a significant improvement in RR and HR detection accuracy compared with existing methods.

Index Terms—Heart rate (HR), millimeter-wave (mm-wave) radar, noncontact detection, respiration rate (RR), zero attracting sign exponentially forgetting least mean square (ZA-SEFLMS).



Manuscript received 13 December 2022; revised 13 February 2023; accepted 21 February 2023. Date of publication 3 March 2023; date of current version 14 April 2023. This work was supported in part by the National Natural Science Foundation of China (NSFC) under Grant 62173032 and Grant 62003038, in part by the Foshan Science and Technology Innovation Special Project under Grant BK22BF005, in part by the Regional Joint Fund of the Guangdong Basic and Applied Basic Research Fund under Grant 2022A1515140109, and in part by the Fundamental Research Funds for the Central Universities under Grant FRF-TP-22-014A1. The associate editor coordinating the review of this article and approving it for publication was Dr. Edward Sazonov. (Corresponding author: Wendong Xiao.)

Luyao Liu and Sen Zhang are with the School of Automation and Electrical Engineering, University of Science and Technology Beijing, Beijing 100083, China (e-mail: b20180299@xs.ustb.edu.cn; zhangsen@ustb.edu.cn).

Jie Zhang is with the School of Electronic and Electrical Engineering, University of Leeds, LS2 9JT Leeds, U.K. (e-mail: eenjz@leeds.ac.uk).

Ying Qu is with the Platform Capability Center, China Mobile Information Technology Company Ltd., Beijing 102206, China (e-mail: a18810172617@126.com).

Wendong Xiao is with the School of Automation and Electrical Engineering, University of Science and Technology Beijing, Beijing 100083, China, also with the Beijing Engineering Research Center of Industrial Spectrum Imaging, Beijing 100083, China, and also with the Shunde Innovation School, University of Science and Technology Beijing, Foshan 528399, China (e-mail: wdxiao@ustb.edu.cn).

Digital Object Identifier 10.1109/JSEN.2023.3250500

I. INTRODUCTION

VITAL signs, especially respiration rate (RR) and heart rate (HR), embody rich information that can provide doctors with reliable diagnosis and effective prevention of some potentially fatal diseases [1]. Most of the conventional detection methods for these two vital signs mainly use intelligent wearable sensor or sticky electrode, such as breath belt [2], photoplethysmography (PPG) sensor [3], and electrocardiography (ECG) sensor [4]. Although the detection results are relatively reliable, these methods may cause an uncomfortable experience and additional burden for the subject involved, especially for those special patients with skin allergy and burn [5]. Acoustic signal is another potential solution for vital sign detection, but its sensing range is limited [6]. Moreover, computer vision-based vital sign detection is sensitive to the lighting and line-of-sight (LoS) conditions, which does not perform well in smoky, poor illumination, or obscured conditions, and may also result in privacy breach [7].

Fortunately, radio frequency (RF)-based vital sign detection can overcome the drawbacks of the aforementioned techniques, which could detect the RR and HR in a

noncontact manner by sensing the repetitive chest wall movement caused by heartbeat and respiration. Recently, Wi-Fi signals could be extracted from commodity devices and Wi-Fi-based noncontact sensing has attracted more attention in numerous applications, such as respiration detection [8], [9], location estimation [10], [11], and gesture recognition [12]. However, the performance of the 2.4-/5-GHz Wi-Fi is limited due to the narrow bandwidth, small antenna number, and large wavelength. Especially for HR detection, it is difficult to capture the tiny phase change caused by heartbeat because the wavelength of 2.4-/5-GHz Wi-Fi (60–120 mm) is much larger than the chest wall displacement due to heartbeat (0.2–0.5 mm [13]). Continuous-wave (CW) Doppler radar, ultrawideband (UWB) pulse radar, and frequency-modulated CW (FMCW) radar are three types of radar commonly used for vital sign detection. CW Doppler radar has a simple radio structure and low power consumption, but it cannot provide the range information of the subject [5]. Thus, its performance is easily affected by clutter interference, leading to poor vital sign detection accuracy. In contrast, UWB pulse radar and FMCW radar have the ability to measure the distance between the subject and the device and occupy a wide bandwidth [14]. However, a wide bandwidth for UWB pulse radar leans on accurate control on the pulsewidth and the radar peak signal strength, resulting in high hardware cost and system complexity [15]. Millimeter-wave (mm-wave) radar is a type of radar technology with the electromagnetic spectrum corresponding to frequencies band of 30–300 GHz, which has a wide bandwidth, narrow beamwidth, and small size [5]. FMCW mm-wave radar integrates the advantages of FMCW and mm-wave technologies. The range resolution is significantly improved due to the wider bandwidth, which helps to isolate the reflections from different objects [16]. Meanwhile, FMCW mm-wave radar has the potential to be with small size due to the higher carrier frequency [5], [17].

Some signal processing techniques have been employed to estimate RR and HR from the received echo signals. Most of the existing works attempt to directly utilize frequency-domain transform techniques, e.g., fast Fourier transform (FFT) [18], short-time Fourier transform (STFT) [19], and CW transform (CWT) [20], or time-domain signal processing techniques, e.g., ensemble empirical mode decomposition (EEMD) [21], autocorrelation [22], and adaptive filter [23], to estimate RR and HR. With these efforts, the RR detection can function well in simple and controlled scenarios. However, it is difficult to accurately detect HR due to the interference of respiration harmonics, noise, and clutter. Specifically, there may be a variety of objects (e.g., wall, door, desk, and furniture) in the environment, so the reflected signal contains much clutter that may overwhelm the heartbeat signal. Moreover, the chest wall displacement caused by respiration can be an order of magnitude higher than that caused by heartbeat, and it is not a pure sine wave, including several significant harmonic components. The respiration harmonics may fall close to or even overwhelm the heartbeat signal, leading to incorrect peak selection. Therefore, it is challenging to achieve accurate and reliable HR detection.

In this article, a noncontact vital sign detection system, named mmRH, is designed for RR and HR detection with an FMCW mm-wave radar, which consists of four functional modules, including the vital sign signal extraction module, the differential enhancement module, the signal decomposition module, and the vital sign rate reconstruction module. First, in the vital sign signal extraction module, the range bin corresponding to the body part with strong vital signs is determined, and then, the vital sign signal is extracted along the slow time, eliminating the clutter interference. Second, the first-order temporal difference is employed to enhance the heartbeat component in the differential enhancement module, alleviating the interference of respiration harmonics and noise. Then, the respiration and heartbeat signals are separated by wavelet packet decomposition (WPD) in the signal decomposition module; thus, the respiration harmonics and high-frequency noise are further suppressed. Finally, in the vital sign rate reconstruction module, the high-resolution sparse spectrum is reconstructed via zero attracting sign exponentially forgetting least mean square (ZA-SEFLMS) algorithm. The frequency bins are significantly increased and the spectral power of respiration harmonics and noise can be further suppressed. Extensive experiments indicate that the designed mmRH could effectively suppress the interference of respiration harmonics, noise, and clutter, and achieve accurate and reliable RR and HR estimation. The main contributions of this article are concluded as follows.

- 1) A prototype of mmRH is designed using an FMCW mm-wave radar for accurate and reliable RR and HR estimation by mitigating the interference of respiration harmonics, noise, and clutter.
- 2) The sparse spectrum reconstruction (SSR) of vital sign rates is mapped into an adaptive filter and the ZA-SEFLMS algorithm is proposed to achieve a high-resolution sparse spectrum, making the peaks associated with RR and HR become dominant.
- 3) Extensive experiments are conducted to evaluate the performance of the designed mmRH under different settings. The experimental results indicate that mmRH could effectively suppress the interference of respiration harmonics, noise, and clutter, and bring a significant improvement in RR and HR detection accuracy compared with existing methods.

The rest of this article is organized as follows. The related works are reviewed in Section II. Preliminaries are given in Section III. Section IV describes the designed system in detail. Experimental results are reported in Section V, followed by some discussions in Section VI. The conclusions are given in Section VII.

II. RELATED WORKS

In this section, we will review the recent advances of RF-based vital sign detection from two perspectives, including 2.4-/5-GHz Wi-Fi-based and radar-based solutions.

A. 2.4-/5-GHz Wi-Fi-Based Solutions

Wi-Fi-based solutions employ ubiquitous off-the-shelf Wi-Fi devices to detect vital signs in a contactless manner.

Received signal strength (RSS) is one of the most commonly used Wi-Fi signals. UbiBreathe was proposed for RR estimation and apnea detection based on RSS [24]. However, RSS is unstable and not sensitive to the micro chest wall movement. Recently, fine-grained channel state information (CSI) is accessible for respiration detection [8], [9], [25], [26]. For example, Li et al. [25] proposed DiverSense, which could push the sensing range of respiration to 40 m by combining sensing signal received from all subcarriers and all antennas in the array. Wang et al. [26] proposed a novel solution to monitor the RR of multiple persons without providing advance information on crowd numbers and assuming that different users have distinct RRs. Passive Wi-Fi radar was also proposed to capture ambient Wi-Fi signals for human sensing [27], [28]. Li et al. [27] utilized the cross ambiguity function to calculate the Doppler information that was used to extract the respiration signal. Although there are several excellent works on Wi-Fi-based RR detection, Wi-Fi-based HR detection is still a challenge because the wavelength of 2.4-/5-GHz Wi-Fi (60–120 mm) is much larger than that of the chest wall displacement due to heartbeat (0.2–0.5 mm [13]).

B. Radar-Based Solutions

To overcome the limitations of Wi-Fi-based solutions, numerous researchers try to employ radar for vital sign detection. Radar-based solutions can be mainly divided into the following three categories according to the technology used.

- 1) CW Doppler radar transmits continuous signals with a constant frequency and amplitude, and the received echo signals are processed to estimate RR and HR [29], [30], [31], [32]. The synchrosqueezing transform-based algorithm was proposed to obtain a concentrated time–frequency distribution for high-resolution instantaneous RR and HR estimation [1]. Li and Lin [33] proposed a wavelet transform-based data length variation technique to distinguish the respiration harmonics from heartbeat signals. CW Doppler radar is known for its low power consumption and simple radio architecture. However, it cannot offer range information so that the performance of vital sign detection is easily susceptible to clutter interference.
- 2) UWB pulse radar transmits pulses with short duration, occupying a wide bandwidth. It can provide range information by measuring the time delay of reflected signals [5], [14], [22], [34]. The two-layer ensemble empirical mode decomposition (TEEMD) approach was proposed to separate the small heartbeat signal from the large respiration signal [21]. Zhang et al. [35] proposed harmonic multiple loop detection (HMLD) algorithm for RR and HR estimation. With a wide bandwidth, the UWB pulse radar can significantly alleviate clutter interference for RR and HR estimation. However, the wide bandwidth will result in high hardware cost and system complexity due to its accurate control on the pulsewidth and the peak signal intensity.
- 3) FMCW radar transmits continuous signals modulated with a linear frequency within a wide bandwidth, which

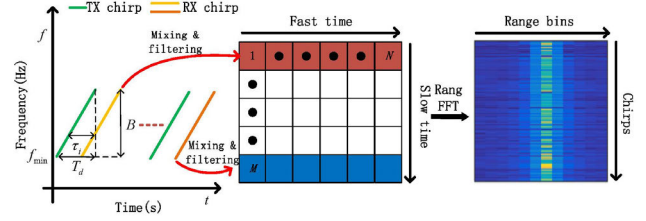


Fig. 1. FMCW radar signal.

can directly measure the range between the subject and the device [36], [37], [38]. Vital-Radio was presented for RR and HR estimation without body contact [16], which can alleviate clutter interference by isolating signals reflected off different objects. Alizadeh et al. [19] applied two bandpass filters to decompose the phase signal to obtain respiration and heartbeat signals and employed STFT to estimate RR and HR. A double-parameter least mean square (LMS) filter was proposed to separate the respiration and heartbeat signals from the phase signal [23]. Sun et al. [39] proposed an adaptive identification EEMD for joint-range spectral estimation to detect HR. Wang et al. [40] designed a heartbeat extractor based on variational mode decomposition (VMD) to extract the heartbeat and respiration signals from the phase signal.

Most of these works directly utilize frequency-domain transform techniques or time-domain signal processing techniques to estimate RR and HR simultaneously. These approaches can perform the RR estimation well in simple and controlled conditions, but they are easy to fail for HR estimation because it is difficult to filter out and separate the interference from respiration harmonics, noise, and clutter. Differently, we present mmRH, a noncontact vital sign detection system, to suppress the interference of respiration harmonics, noise, and clutter. It builds upon an FMCW mm-wave radar named T79 with two transmitted antennas and four received antennas. mmRH can locate the range bin corresponding to the body part with strong vital signs. Furthermore, it can enhance the heartbeat component and reduce the impacts of respiration harmonics and noise on HR estimation by the first-order temporal difference. To further alleviate the interference of respiration harmonics and high-frequency noise, mmRH separates respiration and heartbeat signals by WPD. Finally, mmRH obtains the high-resolution sparse spectrum by ZA-SEFLMS to achieve accurate and reliable RR and HR estimation.

III. PRELIMINARIES

FMCW radar transmits a series of waveforms named chirps, whose frequency increases linearly with time as shown in Fig. 1 and can be expressed as

$$f(t) = f_{\min} + \frac{B}{T_d}t \quad (1)$$

where f_{\min} is the start frequency, B is the bandwidth, and T_d is the duration. The transmitted signal $x_T(t)$ can be

expressed as

$$\begin{aligned} x_T(t) &= A_T \cos \left(2\pi \int_0^t f(\tau) d\tau + \varphi \right) \\ &= A_T \cos \left(2\pi f_{\min} t + \pi \frac{B}{T_d} t^2 + \varphi \right) \end{aligned} \quad (2)$$

where A_T is the amplitude of the transmitted signal and φ is the phase noise. The transmitted signal will be reflected when it encounters multiple subjects in the field of radar view. The echo signal $x_R(t)$ is

$$x_R(t) = A_R \sum_{i=1}^{\Omega} \cos \left[2\pi f_{\min} (t - \tau_i) + \pi \frac{B}{T_d} (t - \tau_i)^2 + \varphi \right] \quad (3)$$

where A_R is the amplitude of the echo signal; τ_i is the round-trip time delay caused by the reflection of the subject in the i th range bin, which can be denoted as $\tau_i = (2d_i(t)/c)$, in which $d_i(t)$ represents the range between the subject in the i th range bin and the radar and c is the speed of light. The echo signal is mixed with a copy of the transmitted signal, and then, the mixed signal is processed by a low-pass filter to obtain the intermediate frequency (IF) signal $x_{IF}(t)$, which can be written as

$$x_{IF}(t) = \frac{A_T A_R}{2} \sum_{i=1}^{\Omega} \cos \left(2\pi \frac{B\tau_i}{T_d} t + 2\pi f_{\min} \tau_i - \pi \frac{B}{T_d} \tau_i^2 + \Delta\varphi \right) \quad (4)$$

where the residual phase noise $\Delta\varphi$ is negligible for short-range radar applications due to the range-correlation effect, and the term $\pi(B/T_d)\tau_i^2$ is also negligible because (B/T_d) is in 10^{12} Hz/s order, while τ_i is in 1 ns; thus, the term is in the order of 10^{-6} . The I -channel IF signal $x_I(t)$ and the Q -channel IF signal $x_Q(t)$ are expressed as

$$x_I(t) = \frac{A_T A_R}{2} \sum_{i=1}^{\Omega} \cos \left(4\pi \frac{Bd_i(t)}{cT_d} t + 4\pi \frac{d_i(t)}{\lambda} \right) \quad (5)$$

$$x_Q(t) = \frac{A_T A_R}{2} \sum_{i=1}^{\Omega} \sin \left(4\pi \frac{Bd_i(t)}{cT_d} t + 4\pi \frac{d_i(t)}{\lambda} \right) \quad (6)$$

where λ denotes the wavelength of the chirp. The complex IF signal $y(t)$ can be expressed as

$$\begin{aligned} y(t) &= x_I(t) + j * x_Q(t) \\ &= \frac{A_T A_R}{2} \sum_{i=1}^{\Omega} \exp \left[j \left(4\pi \frac{Bd_i(t)}{cT_d} t + 4\pi \frac{d_i(t)}{\lambda} \right) \right]. \end{aligned} \quad (7)$$

IV. SYSTEM IMPLEMENTATION

In this section, we detail the designed mmRH system, which consists of four functional modules, as shown in Fig. 2, including the vital sign signal extraction module, the differential enhancement module, the signal decomposition module, and the vital sign rate reconstruction module.

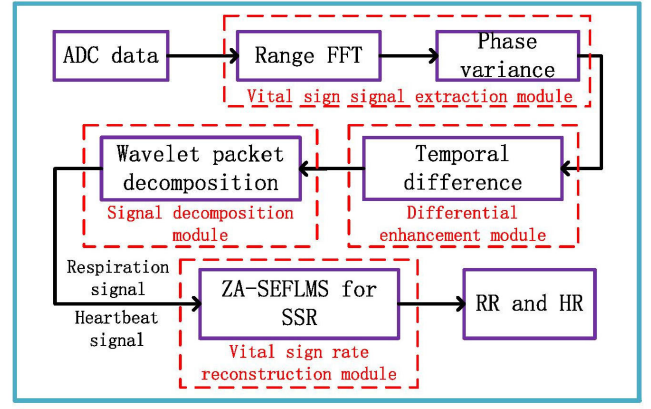


Fig. 2. Overview of mmRH.

A. Vital Sign Signal Extraction Module

The azimuth and elevation of FMCW mm-wave radar used in mmRH are 120° and 30° , respectively. In the field of radar view, the radar signal is sent throughout the spatial environment, where there may be a variety of objects (e.g., wall, door, desk, and furniture), so the reflected signal contains much clutter that may degrade the performance of vital sign detection in mmRH. An FMCW mm-wave radar has the ability to obtain range information, which can isolate reflections from other objects into different range bins.

The complex IF signal $y(t)$ is digitized by an analog-to-digital converter (ADC), and the ADC samples will be stored row by row as shown in Fig. 1, for example, the ADC samples of the IF signal for the first chirp are placed in the first row, the ADC samples of the IF signal for the second chirp are placed in the second row, and so on. The dimension corresponding to N samples per chirp is called the fast time, and the dimension corresponding to M different chirps is called the slow time. Therefore, the digitized complex IF signal $y(n, m)$ can be expressed for the n th ADC sample and the m th chirp as

$$\begin{aligned} y(n, m) &= \frac{A_T A_R}{2} \sum_{i=1}^{\Omega} \exp \left[j \left(2\pi \underbrace{\frac{2Bd_i(nT_f)}{cT_d}}_{f_b} nT_f \right. \right. \\ &\quad \left. \left. + 4\pi \underbrace{\frac{d_i(nT_f + mT_s)}{\lambda}}_{\phi} \right) \right] \end{aligned} \quad (8)$$

where T_f and T_s are the time interval corresponding to the fast time and the slow time, respectively.

The range $d_i(t)$ between the subject in the i th range bin and the radar is

$$d_i(t) = \hat{d}_i + \tilde{d}_i(t) \quad (9)$$

where \hat{d}_i is the constant distance between the subject in the i th range bin and the radar and $\tilde{d}_i(t)$ is the time-varying displacement of the subject. Based on (8) and (9), the frequency

of the m th chirp is expressed as

$$f_b = \frac{2B(\hat{d}_i + \tilde{d}_i(nT_f))}{cT_d} \approx \frac{2B\hat{d}_i}{cT_d} \quad (10)$$

where the displacement $\tilde{d}_i(nT_f)$ in fast time can be neglected because it is tiny during chirp duration and cannot lead to an appreciable change in frequency. The frequency is related to the range of reflecting objects. In order to find the range bins with reflecting objects, an FFT is performed over the fast time for each chirp as shown in Fig. 1, which is called range-FFT

$$z(i, m) = \sum_{n=0}^{N-1} y(n, m) \exp(-j2\pi in/N). \quad (11)$$

The range information obtained by range FFT can be denoted by $z(i, m)$, where i is the range bin index. Note that the range bins with reflecting objects have more energy than those without reflecting objects. Thus, the range FFT can filter out the empty bins, while the residual range bins may correspond to wall, desk, or metal objects. Also, considering that the bandwidth of FMCW mm-wave radar used in the study is 4 GHz, whose range resolution is 3.75 cm, the human subject would be detected across the multirange bins. In other words, the range bins may correspond to the body parts where the vital signs are weak, such as arms or legs. Therefore, to determine whether the information of vital signs exists in the selected range bin, the phase variance of the candidate bins obtained by range FFT is employed in mmRH.

Based on (8) and (9), we have the phase

$$\phi = \frac{4\pi(\hat{d}_i + \tilde{d}_i(nT_f + mT_s))}{\lambda} \approx \frac{4\pi(\hat{d}_i + \tilde{d}_i(mT_s))}{\lambda} \quad (12)$$

where for a quasi-stationary human subject, \hat{d}_i is the distance between the human subject and the radar that remains constant in slow time and $\tilde{d}_i(t)$ is the chest wall displacement caused by respiration and heartbeat. The chest wall displacement $\tilde{d}_i(nT_f)$ in fast time can be neglected due to short chirp duration, while the chest wall displacement $\tilde{d}_i(mT_s)$ in slow time will result in phase change. Therefore, there is a large phase variance for the range bin corresponding to the body part with strong vital signs. However, for the range bin with weak vital signs, the phase variance will be much smaller. The range bin corresponding to the body part with strong vital signs is that whose phase variance is higher than a certain threshold. After determining the range bin corresponding to the body part with strong vital signs, the phase signal $\phi = [\phi_1, \phi_2, \dots, \phi_M]$ can be extracted along the slow time, which includes respiration signal, heartbeat signal, and noise.

B. Differential Enhancement Module

Fig. 3(a) shows the phase signal ϕ and its corresponding spectrum. The waveform with large amplitude is caused by respiration and varies significantly, while the tiny vibration at the top of the waveform is caused by heartbeat, which is weak and not visible. It is apparent that the chest wall displacement is mainly modulated by respiration. The chest wall displacement caused by respiration can be an order of

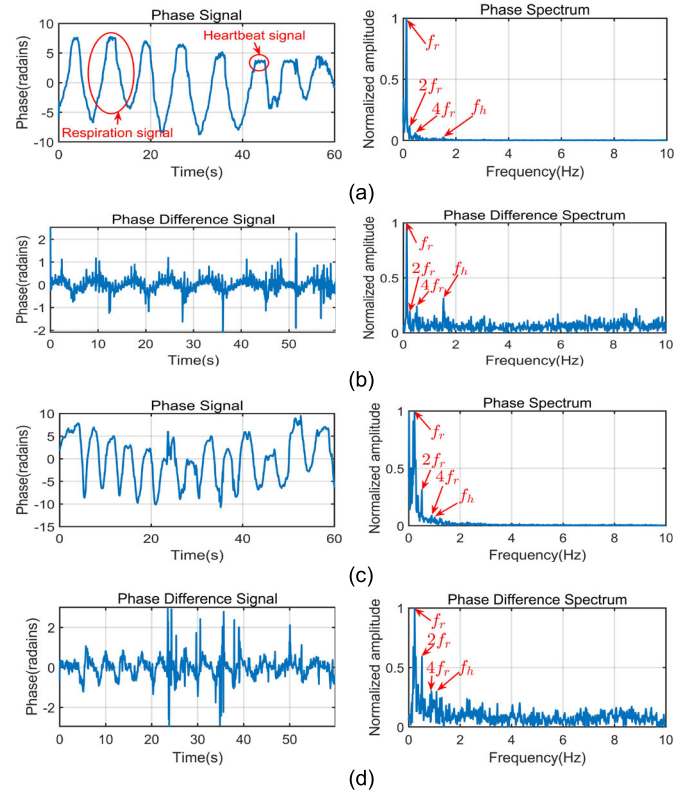


Fig. 3. Examples of phase signal and phase difference signal. (a) and (c) Phase signal and its spectrum. (b) and (d) Phase difference signal and its spectrum.

magnitude higher than that caused by heartbeat. Moreover, it is found that the chest wall displacement caused by respiration is not purely sinusoidal and contains several distinct harmonic components, as shown in the phase spectrum [i.e., the right column of Fig. 3(a)]. Compared with the respiration frequency f_r , the power of the heartbeat frequency f_h is weak and easily submerged in the power of the second respiration harmonic $2f_r$, the fourth respiration harmonic $4f_r$, and noise, leading to an incorrect HR estimation.

In order to alleviate the interference of respiration harmonics and noise on HR estimation, the first-order temporal difference is performed to enhance the heartbeat component of the phase signal after the vital sign signal extraction module, as shown in Fig. 1. The first-order temporal difference of the phase signal ϕ can be expressed as

$$\phi' = [\phi_2 - \phi_1, \phi_3 - \phi_2, \dots, \phi_M - \phi_{(M-1)}]^T. \quad (13)$$

To be consistent with the count of samples in ϕ , i.e., M , the phase difference signal ϕ' is approximated by

$$\phi' = [0, \phi^T]^T. \quad (14)$$

Fig. 3(b) shows the phase difference signal and its corresponding spectrum. It can be seen that the first-order temporal difference can significantly enhance the heartbeat component, and f_h becomes more apparent in the spectrum compared with $2f_r$ and $4f_r$ and noise.

Although the first-order temporal difference can enhance the heartbeat signal, it does not completely eliminate the

impacts of respiration harmonics and noise on HR estimation.

An example is shown in Fig. 3(c) and (d), and it is seen from the spectrum that the power of f_h is enhanced after the differential enhancement module, but it is still lower than that of the respiration harmonics and noise. The frequency corresponding to the peak of the fourth harmonic may be incorrectly selected as heartbeat frequency, leading to a large HR estimation error. In the following modules, the signal decomposition module further suppresses the respiration harmonics and high-frequency noise. Meanwhile, the vital sign rate reconstruction module is presented to obtain a high-resolution sparse spectrum, which helps to accurately detect HR.

C. Signal Decomposition Module

Note that the chest wall movement due to respiration ranges from 1 to 12 mm with a frequency of 0.1–0.5 Hz, while that caused by heartbeat ranges from 0.2 to 0.5 mm with a frequency of 0.8–2.0 Hz [5], [14]. Leveraging this property, we apply WPD to decompose the phase difference signal ϕ' after the differential enhancement module and reconstruct the respiration signal θ and the heartbeat signal \mathbf{h} . The separation of heartbeat and respiration signals can further mitigate the interference of respiration harmonics and high-frequency noise on HR estimation, which can be expressed as

$$\phi' = \mathbf{s}_{g,0} + \mathbf{s}_{g,1} + \mathbf{s}_{g,2} + \dots + \mathbf{s}_{g,2^g-2} + \mathbf{s}_{g,2^g-1} \quad (15)$$

where \mathbf{s} is the subband signal after the g th layer WPD. The frequency range of the q th subband is $(f_{\text{slow}}/2^{g+1})q \sim (f_{\text{slow}}/2^{g+1})(q+1)$, $q = 0, 1, 2, \dots, 2^g - 1$. f_{slow} is a slow time sampling rate.

The Morlet wavelet is chosen as the wavelet basis because its shape is similar to that of the respiration and heartbeat waveforms. In the sixth level of WPD, we can get 64 subband signals

$$\theta = \mathbf{s}_{6,0} + \mathbf{s}_{6,1} + \mathbf{s}_{6,2} \quad (16)$$

$$\mathbf{h} = \mathbf{s}_{6,5} + \mathbf{s}_{6,6} + \mathbf{s}_{6,7} + \mathbf{s}_{6,8} + \mathbf{s}_{6,9} + \mathbf{s}_{6,10} + \mathbf{s}_{6,11}. \quad (17)$$

The first to third subband signals are used to reconstruct θ and the sixth to twentieth subband signals are utilized to reconstruct \mathbf{h} . After WPD, a time window of δ seconds slides on the respiration and heartbeat signals with incremental step of Δ seconds. According to the respiration and heartbeat signals with the sliding time window, the vital sign rate reconstruction module is proposed to obtain high-resolution sparse spectrum for accurate and reliable RR and HR estimation.

D. Vital Sign Rate Reconstruction Module

1) *SSR for Vital Sign Rate Reconstruction*: SSR aims to obtain the high-resolution sparse spectrum by increasing signal sparsity in some typical domains. In this module, the respiration and heartbeat spectrums are reconstructed based on the following underdetermined linear equation:

$$\mathbf{h} = \Psi \mathbf{e} + \eta \quad (18)$$

$$\theta = \Psi \mathbf{w} + \sigma \quad (19)$$

where $\mathbf{e} = [e_1, e_2, \dots, e_L]^T$ and $\mathbf{w} = [w_1, w_2, \dots, w_L]^T$ are $L \times 1$ column vectors, which are unknown solutions of

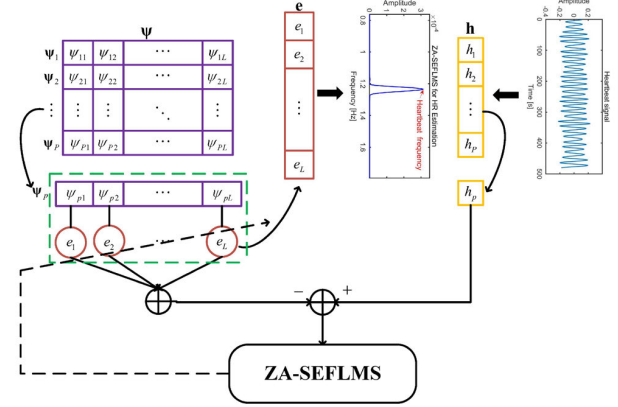


Fig. 4. SSR of vital sign rates based on adaptive filter.

the respiration spectrum and heartbeat spectrum with intrinsic sparsity, respectively. $\mathbf{h} = [h_1, h_2, \dots, h_M]^T$ and $\theta = [\theta_1, \theta_2, \dots, \theta_M]^T$ are $M \times 1$ column vectors ($M \ll L$), which are the respiration signal and heartbeat signal obtained by the signal decomposition module, respectively. η and σ are the noise from the environment and body. Ψ is an $M \times L$ basis matrix whose elements are expressed as

$$\psi_{m,l} = e^{j \frac{2\pi}{L} ml}, \quad m = 1, \dots, M; \quad l = 1, \dots, L. \quad (20)$$

The high-resolution sparse spectrum is reconstructed by the respiration and heartbeat signals and a given matrix. Compared with FFT, the frequency bins of the reconstructed spectrum by SSR are significantly increased. The spectral power of the respiration harmonics and noise is further suppressed with the introduction of sparse constraint, and the peaks related to RR and HR become dominant.

2) *ZA-SEFLMS Algorithm for SSR Based on Adaptive Filter*: Adaptive filter has been widely used because it has a simple structure and performs well in the face of interference. The estimation error $\varepsilon(k)$ of the adaptive filter is denoted as

$$\varepsilon(k) = \rho(k) - \mathbf{v}^T(k) \boldsymbol{\omega}(k) \quad (21)$$

where $\rho(k)$ is the desired signal, k is the time instant, $\boldsymbol{\omega}(k) = [\omega_0(k), \omega_1(k), \dots, \omega_{l-1}(k)]^T$ and $\mathbf{v}(k) = [v(k), v(k-1), \dots, v(k-l+1)]^T$ denote the adaptive filter coefficient vector and input vector, respectively, and l is the filter length.

In this module, we map the SSR of vital sign rates to the adaptive filter framework, as shown in Fig. 4. $\psi_m = [\psi_{m1}, \psi_{m2}, \dots, \psi_{mL}]$, $m \in \{1, 2, \dots, M\}$, is the row vectors of Ψ , which corresponds to the input vector $\mathbf{v}^T(k)$ of the adaptive filter. The element h_m , $m \in \{1, 2, \dots, M\}$, in \mathbf{h} corresponds to the desired signal $\rho(k)$. The vector $\mathbf{e} = [e_1, e_2, \dots, e_L]^T$ corresponds to the adaptive filter coefficient vector $\boldsymbol{\omega}(k)$. The correspondences of parameters between the SSR and the adaptive filter are summarized in Table I. To train \mathbf{e} into convergence, the row vectors of Ψ and the corresponding elements of \mathbf{h} are used recursively.

Without loss of generality, we take the SSR of HR as an example to detail the proposed ZA-SEFLMS algorithm.

TABLE I

CORRESPONDENCES BETWEEN THE PARAMETERS OF SSR AND THOSE OF THE ADAPTIVE FILTER

SSR	Adaptive Filter
\mathbf{e}	$\mathbf{w}(k)$
Ψ_m	$\mathbf{v}^T(k)$
h_m	$\rho(k)$

Recursive least square (RLS) has attracted more attention in recent years, whose cost function is defined as the weighted sum of continuous squared error sequence. According to the correspondences in Table I, the cost function of SSR is defined as

$$\xi_{\text{RLS}}(k) = \sum_{u=1}^k \beta^{k-u} |\eta(u)|^2 \quad (22)$$

where $0 \leq \beta < 1$ is the forgetting factor, $\eta(u) = h_m - \Psi_m \mathbf{e}(k)$ is the recursion error of SSR, $m = \text{mod}(u, M) + 1$, and $\text{mod}(\cdot)$ denotes the remainder function.

Since the standard RLS algorithm cannot directly generate sparse solutions, it is necessary to introduce the sparse penalty function, which can be achieved by using the $L1$ norm $\|\mathbf{e}(k)\|_1$ of $\mathbf{e}(k)$. The complete expression of the novel cost function is shown as follows:

$$\xi_{\text{ZA-EFLMS}}(k) = \sum_{u=1}^k \beta^{k-u} |\eta(u)|^2 + \gamma \|\mathbf{e}(k)\|_1 \quad (23)$$

where γ is a regularization parameter that aims to counterbalance the gradient correction and sparse constraint.

The gradient descent recursion of the heartbeat signal spectrum vector is

$$\begin{aligned} \nabla &= \frac{\partial \xi_{\text{ZA-EFLMS}}(k)}{\partial \mathbf{e}(k)} \\ &= -2 \sum_{u=1}^k \beta^{k-u} \Psi_m (h_m - \Psi_m \mathbf{e}(k)) + \gamma \text{sgn}(\mathbf{e}(k)) \\ &= -2 \sum_{u=1}^k \beta^{k-u} \Psi_m \eta(u) + \gamma \text{sgn}(\mathbf{e}(k)) \end{aligned} \quad (24)$$

$$\begin{aligned} \mathbf{e}(k+1) &= \mathbf{e}(k) + \frac{1}{2} \mu (-\nabla) \\ &= \mathbf{e}(k) + \mu \Theta \Lambda \eta(k) - \varsigma \text{sgn}(\mathbf{e}(k)) \end{aligned} \quad (25)$$

where

$$\Theta = [\alpha_1, \alpha_2, \dots, \alpha_k] \quad (26)$$

$$\alpha_u = [\psi_{m1}, \psi_{m2}, \dots, \psi_{mL}], \quad u \in \{1, 2, \dots, k\} \quad (26)$$

$$\Lambda = \text{diag} \{ \beta^{k-1}, \beta^{k-2}, \dots, 1 \} \quad (27)$$

$$\eta(k) = [\eta(1), \eta(2), \dots, \eta(k)]^T \quad (28)$$

μ is a step size, and $\varsigma = \gamma \mu$ is a zero attraction factor. The $\text{sgn}(\cdot)$ is a componentwise sign function defined as

$$\text{sgn}(\kappa) = \begin{cases} \frac{\kappa}{|\kappa|}, & \text{if } \kappa \neq 0 \\ 0, & \text{otherwise.} \end{cases} \quad (29)$$

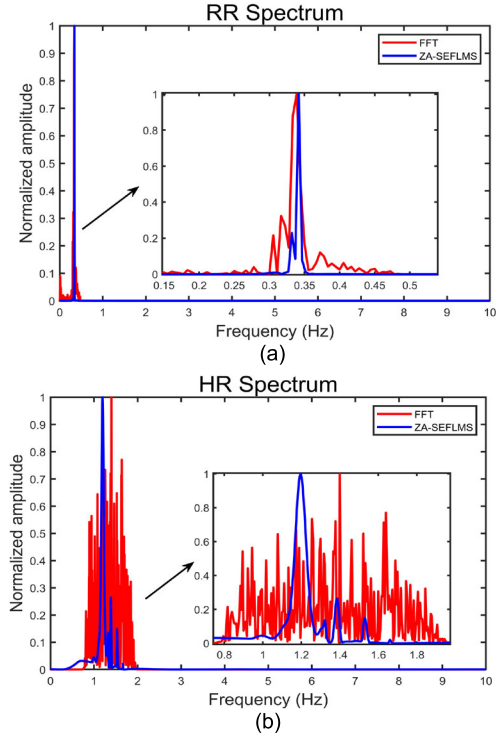


Fig. 5. Spectrum comparisons between FFT and ZA-SEFLMS. (a) RR spectrum. (b) HR spectrum.

Some noise could cause pulse interference, which may degrade the performance of vital sign detection due to the unstable gradient descent. In order to suppress the sudden pulse interference, the $\text{sgn}(\cdot)$ function is applied to restrict the recursion error $\eta(k)$. As a result, the novel recursion updating equation is obtained

$$\begin{aligned} \mathbf{e}(k+1) &= \mathbf{e}(k) + \frac{1}{2} \mu (-\nabla) \\ &= \mathbf{e}(k) + \mu \Theta \Lambda \text{sgn}(\eta(k)) - \varsigma \text{sgn}(\mathbf{e}(k)). \end{aligned} \quad (30)$$

Finally, a reconstructed heartbeat spectrum $|\mathbf{e}(k)|^2$ could be obtained by an iterative calculation based on (30). Similarly, the respiration spectrum $|\mathbf{w}(k)|^2$ could also be obtained. In Fig. 5(a), it can be seen that the RR estimation results between FFT and ZA-SEFLMS are consistent and accurate. However, the spectrum of FFT is contaminated by noise, while that obtained by ZA-SEFLMS is sparse and clean. The comparison of HR estimation results between FFT and ZA-SEFLMS is shown in Fig. 5(b). Based on the ground truth, it can be found that the frequency corresponding to the highest peak of the FFT spectrum is not heartbeat frequency but the frequency of the third respiration harmonic. Meanwhile, the FFT spectrum suffers from interference caused by noise from the environment and body. Accordingly, the frequency corresponding to the peak of respiration harmonics or noise may be incorrectly selected as heartbeat frequency, leading to a large HR estimation error. In contrast, the spectrum of ZA-SEFLMS is clean and sparse, and the spectral power of respiration harmonics and noise is generally 0 or close to 0. As a result, the peak corresponding to HR becomes dominant.



Fig. 6. Illustration of the experimental scene used for human vital sign detection.

V. PERFORMANCE EVALUATION

In this section, we verify the performance of the proposed mmRH in different settings, including the distance between the subject and the radar, the sensor position, and the user heterogeneity. Wavelet analysis and autocorrelation computation (WAAC) [20], TEEMD [21], and rigrsure adaptive soft threshold noise reduction based on discrete wavelet transform (RA-DWT) [38] are considered as baseline methods in the experiments.

A. Experimental Settings

In mmRH, the start frequency f_{\min} is 76.4 GHz, and the duration T_d of a chirp is 48 μ s. The slow time sampling rate f_{slow} is 20 Hz, and the fast time sampling rate f_{fast} is 3.2 MHz. The bandwidth B of each chirp is 4 GHz. The time window of $\delta = 16$ s slides on the respiration signal with an incremental step of $\Delta = 2$ s. For the heartbeat signal, $\delta = 8$ s and $\Delta = 2$ s. The parameters of the proposed ZA-SEFLMS are chosen as: $\mu = 1 \times 10^{-5}$, $k = 5 \times 10^3$, and $\zeta = 2 \times 10^{-6}$.

All the experiments are conducted in a typical indoor office environment, as shown in Fig. 6. The HKH-11C pressure sensor is employed to acquire RR and the PPG sensor is used to obtain HR.

B. Experimental Results

We first present the experimental results of mmRH for RR and HR estimation. To evaluate the performance of mmRH, the average absolute error (AAE), the AAE percentage (AAEP), and the Pearson correlation coefficient r are considered, which are defined as

$$\text{AAE} = \frac{1}{\varpi} \sum_{o=1}^{\varpi} |p_e(o) - p_t(o)| \quad (31)$$

$$\text{AAEP} = \frac{1}{\varpi} \sum_{o=1}^{\varpi} \frac{|p_e(o) - p_t(o)|}{p_t(o)} \quad (32)$$

$$r = \frac{\sum_{o=1}^{\varpi} (p_e(o) - \bar{p}_e)(p_t(o) - \bar{p}_t)}{\sqrt{\sum_{o=1}^{\varpi} (p_e(o) - \bar{p}_e)^2 \sum_{o=1}^{\varpi} (p_t(o) - \bar{p}_t)^2}} \quad (33)$$

where ϖ is the total number of time windows during the observation time and $p_t(o)$ and $p_e(o)$ are the ground truth and the estimation result in the o th time window, respectively.

During the experiment, the human subject sits in a chair 1.0 m away from the radar and keeps normal respiration. The 9-min instantaneous trajectories of RR and HR are shown in Fig. 7(a) and (c), respectively. It could be found that

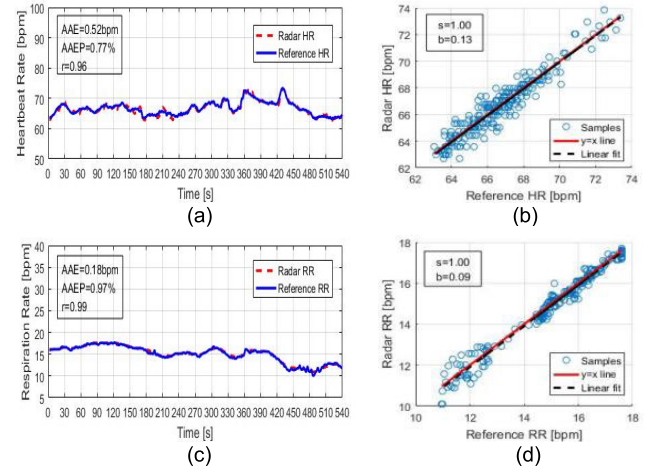


Fig. 7. Comparisons between radar results and reference sensor results. (a) Instantaneous trajectory of HR. (b) Radar HR versus reference sensor HR. (c) Instantaneous trajectory of RR. (d) Radar RR versus reference sensor RR.

the instantaneous trajectories of RR and HR extracted from mmRH show high consistency and reliability compared with the ground truth of the reference sensor. Furthermore, the sample points cloud between the radar and the reference sensor is shown in Fig. 7(b) and (d). Optimally, all the samples are distributed on the “ $y = x$ ” line, indicating that the radar result is equivalent to the ground truth of the reference sensor. RR data follow a similar linear pattern around “ $y = x$ ” line with a slope of 1.00 and a deviation of 0.09. Similarly, the slope of the linear fit curve for the HR data is 1.00 with a deviation of 0.13. The curve fit between the radar data and the ground truth of the reference sensor is similar to the “ $y = x$ ” line, which indicates the reliability of the RR and HR detection of mmRH.

C. Effects of Distance

In this section, it investigates the effects of the distance between the FMCW mm-wave radar and the human subject on RR and HR estimation. Volunteers face the radar at different distances, as shown in Fig. 8(a). The absolute errors of RR and HR estimation are shown in Fig. 8(b) and (c), respectively. The asterisk in Fig. 8(b) and (c) represents the mean of the absolute error. The mean error for HR estimation of mmRH increases from 0.27 to 2.16 beats per minute (BPM) with the increment of the distance from 0.5 to 3.0 m. For RR estimation, it can be found that the mean error of mmRH is within 0.15 BPM when the distance is less than 1.5 m. The mean error increases to 0.39 BPM with the increase in distance to 3 m. As a result, we can find that the performance of mmRH degrades with the increment of the distance due to the reduction of signal-to-noise ratio (SNR). Compared with the heartbeat signal, the respiration signal has a higher SNR, so there is less degradation for RR estimation with increasing distance. Furthermore, we compare the performance of mmRH with WAAC [20], TEEMD [21], and RA-DWT [38]. It can be seen that mmRH achieves better performance.

D. Effects of Sensor Position

In this section, it investigates the effects of sensor position on RR and HR estimation, where the FMCW mm-wave radar

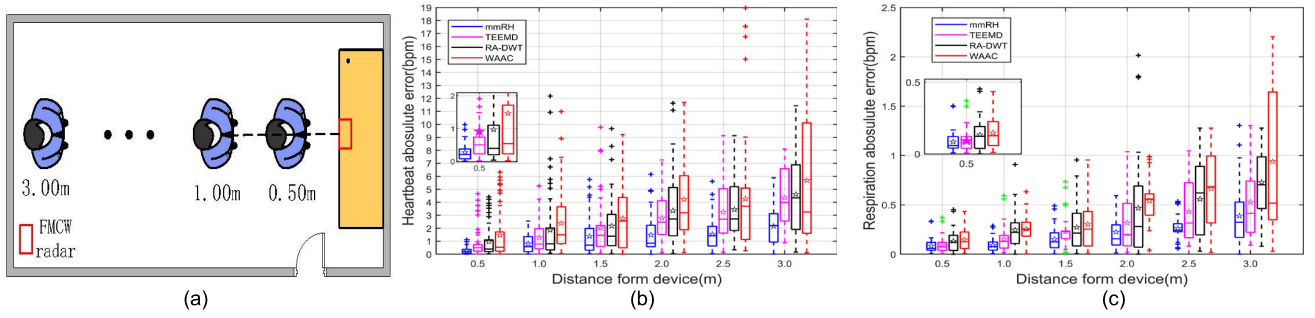


Fig. 8. Experimental scenario description and results of different distances. (a) Experimental scenario description. (b) Absolute error of HR estimation. (c) Absolute error of RR estimation.

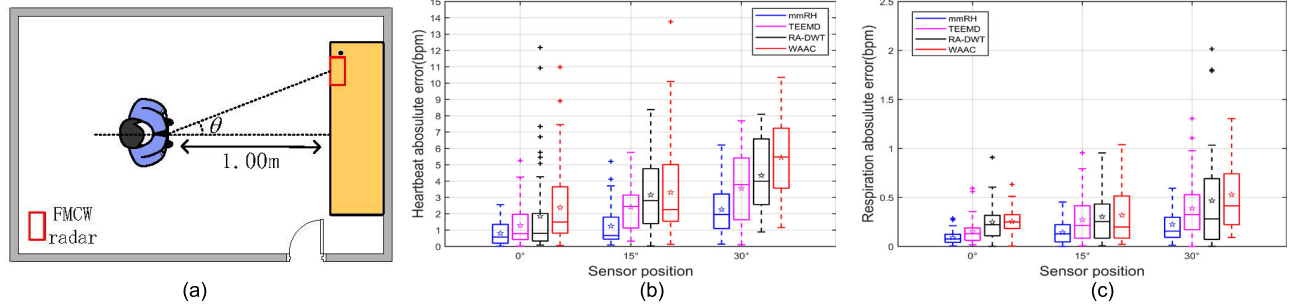


Fig. 9. Experimental scenario description and results of different sensor positions. (a) Experimental scenario description. (b) Absolute error of HR estimation. (c) Absolute error of RR estimation.

is placed at angles 0° , 15° , and 30° , as shown in Fig. 9(a). The estimation results of RR and HR with different sensor positions are shown in Fig. 9(b) and (c), respectively. The asterisk in Fig. 9(b) and (c) represents the mean error. It can be seen that for both RR and HR estimation, the mean error increases with increasing angle. The main reason is that as the angle between the human subject and the radar becomes larger, the SNR of the reflected signal becomes smaller and smaller. However, the performance of RR estimation is better than HR due to its high SNR. Furthermore, it is apparent that the mmRH performs better than other methods, especially for HR estimation.

E. Effects of User Heterogeneity

In this section, it investigates the effects of user heterogeneity on RR and HR estimation of mmRH. The experiment is conducted on ten different volunteers (five males and five females). The RR and HR estimation results are shown in Fig. 10(a) and (b), respectively. The asterisk in Fig. 10(a) and (b) represents the mean of the absolute error. According to Fig. 10(a), the maximum mean error is less than 0.74 BPM for all volunteers. Similarly, it can be seen from Fig. 10(b) that the mean error for all volunteers is within 0.25 BPM.

VI. DISCUSSION

The effects of respiration harmonic interference on HR estimation are shown with real examples in Fig. 3(a). It is apparent that the chest wall displacement caused by heartbeat is much smaller than that caused by respiration. Moreover, the chest wall displacement due to respiration is not an ideal sinusoidal signal, which includes several significant harmonic

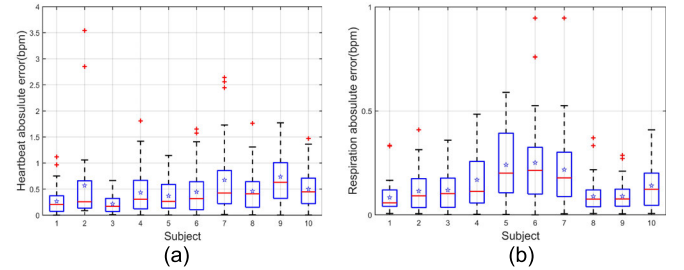


Fig. 10. Estimation results of different users. (a) HR estimation result. (b) RR estimation result.

components, as shown in the phase signal spectrum [i.e., the right column of Fig. 3(a)]. The weak heartbeat component suffers from the interference from the second respiration harmonic $2f_r$, the fourth respiration harmonic $4f_r$, and noise. Unfortunately, for some common frequency-domain and time-domain methods [18], [19], [20], [21], [22], [23], it is challenging to filter out or separate the respiration harmonics in the heartbeat signal. Thus, these methods may easily fail to accurately detect HR, especially when the respiration harmonics are strong and fall close to HR. According to Fig. 5(b), the frequency of the fourth respiration harmonic is incorrectly selected as heartbeat frequency in the FFT spectrum, leading to a large HR estimation error. As shown in Fig. 3(b), the heartbeat component is enhanced and the heartbeat frequency f_h becomes more apparent after the first-order difference. It should be noted that the first-order difference does not completely eliminate the impacts of respiration harmonics and noise [see Fig. 3(c) and (d)]. In what follows, WPD is employed to separate respiration and heartbeat signals, thus further suppressing the interference of respiration harmonics

and high-frequency noise. Furthermore, ZA-SEFLMS is proposed to obtain a high-resolution sparse spectrum, making the peak corresponding to HR dominant. As shown in Fig. 5(b), the spectrum obtained by ZA-SEFLMS is clean and sparse because the spectral power of respiration harmonics and noise can be further suppressed with the introduction of sparse constraint, and the peak related to HR becomes dominant.

The RR and HR instantaneous trajectories and the sample points cloud between the radar and the reference sensor show high agreement and reliability (see Fig. 8). Furthermore, according to Fig. 9, mmRH achieves better performance than WAAC [20], TEEMD [21], and RA-DWT [38]. In particular, for HR detection, the performance gap between mmRH and other methods becomes larger as the distance increases. Similarly, mmRH performs better compared with other methods with the increment of the angle, especially for HR estimation. The main reason is that mmRH improves the SNR of heartbeat signals by mitigating the interference of respiration harmonics, noise, and clutter. Specifically, mmRH locates the range bin corresponding to body part with strong vital signs to extract vital sign signals, eliminating the clutter interference. Then, it reduces the interference of respiration harmonics and noise by the first-order difference and WPD. Finally, it obtains a high-resolution sparse spectrum by ZA-SEFLMS to estimate RR and HR.

The designed mmRH could effectively suppress the respiration harmonic, noise, and clutter interference and achieve accurate and reliable RR and HR estimation. It should be noted that this study only examined the effects of respiration harmonics, noise, and clutter on RR and HR estimation. There are still some challenges that need to be addressed in the future, including the interference of random body movements, multiperson vital sign detection, and long-distance vital sign detection.

VII. CONCLUSION

In this article, mmRH, a system that achieves noncontact vital sign detection using an FMCW mm-wave radar, is designed, which consists of four functional modules. The vital sign signal extraction module is designed to locate the range bin corresponding to the body part with strong vital signs, eliminating the clutter interference. The differential enhancement module and the signal decomposition module are presented to reduce the interference of respiration harmonics and noise. In the vital sign rate reconstruction module, a ZA-SEFLMS algorithm is proposed to estimate RR and HR, which effectively develops the sparsity of the spectrum, increases the frequency bins, and promotes the reconstruction of the dominant vital sign rates. Extensive experiments are conducted to evaluate the performance of mmRH under different settings, including the distance between the human subject and the radar, the sensor position, and the user heterogeneity. Experimental results indicate that mmRH could effectively suppress the respiration harmonics, noise, and clutter interference to achieve accurate and reliable vital sign detection. Furthermore, mmRH could significantly improve the vital sign detection accuracy compared with existing methods.

REFERENCES

- [1] H. Zhao, H. Hong, L. Sun, Y. Li, C. Li, and X. Zhu, "Noncontact physiological dynamics detection using low-power digital-IF Doppler radar," *IEEE Trans. Instrum. Meas.*, vol. 66, no. 7, pp. 1780–1788, Jul. 2017.
- [2] E. Piuze, S. Pisa, E. Pittella, L. Podestà, and S. Sangiovanni, "Wearable belt with built-in textile electrodes for cardio-Respiratory monitoring," *Sensors*, vol. 20, no. 16, p. 4500, Aug. 2020.
- [3] J. I. Rodriguez-Labra et al., "Development of a PPG sensor array as a wearable device for monitoring cardiovascular metrics," *IEEE Sensors J.*, vol. 21, no. 23, pp. 26320–26327, Dec. 2021.
- [4] J. Lazaro et al., "Electrocardiogram derived respiratory rate using a wearable armband," *IEEE Trans. Biomed. Eng.*, vol. 68, no. 3, pp. 1056–1065, Mar. 2021.
- [5] A. Singh, S. U. Rehman, S. Yongchareon, and P. H. J. Chong, "Multi-resident non-contact vital sign monitoring using radar: A review," *IEEE Sensors J.*, vol. 21, no. 4, pp. 4061–4084, Nov. 2021.
- [6] T. Wang, D. Zhang, Y. Zheng, T. Gu, X. Zhou, and B. Dorizzi, "C-FMCW based contactless respiration detection using acoustic signal," *Proc. ACM Interact., Mobile, Wearable Ubiquitous Technol.*, vol. 1, no. 4, pp. 1–20, 2018.
- [7] J. Zhang, Y. Li, and W. Xiao, "Integrated multiple kernel learning for device-free localization in cluttered environments using spatiotemporal information," *IEEE Internet Things J.*, vol. 8, no. 6, pp. 4749–4761, Mar. 2021.
- [8] X. Liu, J. Cao, S. Tang, J. Wen, and P. Guo, "Contactless respiration monitoring via off-the-shelf WiFi devices," *IEEE Trans. Mobile Comput.*, vol. 15, no. 10, pp. 2466–2479, Oct. 2015.
- [9] Y. Zeng, D. Wu, J. Xiong, J. Liu, Z. Liu, and D. Zhang, "MultiSense: Enabling multi-person respiration sensing with commodity WiFi," *Proc. ACM Interact., Mobile, Wearable Ubiquitous Technol.*, vol. 4, no. 3, pp. 1–29, Sep. 2020.
- [10] J. Zhang, W. Xiao, and Y. Li, "Data and knowledge twin driven integration for large-scale device-free localization," *IEEE Internet Things J.*, vol. 8, no. 1, pp. 320–331, Jan. 2021.
- [11] J. Zhang, Y. Li, W. Xiao, and Z. Zhang, "Online spatiotemporal modeling for robust and lightweight device-free localization in nonstationary environments," *IEEE Trans. Ind. Inform.*, pp. 1–11, 2022.
- [12] K. Ali, A. X. Liu, W. Wang, and M. Shahzad, "Recognizing keystrokes using WiFi devices," *IEEE J. Sel. Areas Commun.*, vol. 35, no. 5, pp. 1175–1190, May 2017.
- [13] G. Ramachandran and M. Singh, "Three-dimensional reconstruction of cardiac displacement patterns on the chest wall during the P, QRS and T-segments of the ECG by laser speckle interferometry," *Med. Biol. Eng. Comput.*, vol. 27, no. 5, pp. 525–530, Sep. 1989.
- [14] T. Zheng, Z. Chen, S. Ding, and J. Luo, "Enhancing RF sensing with deep learning: A layered approach," *IEEE Commun. Mag.*, vol. 59, no. 2, pp. 70–76, Feb. 2021.
- [15] J. C. Y. Lai et al., "Wireless sensing of human respiratory parameters by low-power ultrawideband impulse radio radar," *IEEE Trans. Instrum. Meas.*, vol. 60, no. 3, pp. 928–938, Mar. 2011.
- [16] F. Adib, H. Mao, Z. Kabelac, D. Katabi, and R. C. Miller, "Smart homes that monitor breathing and heart rate," in *Proc. 33rd Annu. ACM Conf. Hum. Factors Comput. Syst.*, Apr. 2015, pp. 837–846.
- [17] A. Arbabian, S. Callender, S. Kang, M. Rangwala, and A. M. Niknejad, "A 94 GHz mm-Wave-to-baseband pulsed-radar transceiver with applications in imaging and gesture recognition," *IEEE J. Solid-State Circuits*, vol. 48, no. 4, pp. 1055–1071, Apr. 2013.
- [18] J. Tu and J. Lin, "Fast acquisition of heart rate in noncontact vital sign Radar measurement using time-window-variation technique," *IEEE Trans. Instrum. Meas.*, vol. 65, no. 1, pp. 112–122, Jan. 2016.
- [19] M. Alizadeh, G. Shaker, J. C. M. De Almeida, P. P. Morita, and S. Safavi-Naeini, "Remote monitoring of human vital signs using mm-Wave FMCW radar," *IEEE Access*, vol. 7, pp. 54958–54968, 2019.
- [20] L. Liu, S. Zhang, and W. Xiao, "Noncontact vital signs detection using joint wavelet analysis and autocorrelation computation," *Chin. J. Eng.*, vol. 43, no. 9, pp. 1206–1214, 2021.
- [21] K.-K. Shyu, L.-J. Chiu, P.-L. Lee, T.-H. Tung, and S.-H. Yang, "Detection of breathing and heart rates in UWB radar sensor data using FVPIEF-based two-layer EEMD," *IEEE Sensors J.*, vol. 19, no. 2, pp. 774–784, Jan. 2019.
- [22] H. Shen et al., "Respiration and heartbeat rates measurement based on autocorrelation using IR-UWB radar," *IEEE Trans. Circuits Syst. II, Exp. Briefs*, vol. 65, no. 10, pp. 1470–1474, Oct. 2018.

- [23] M. He, Y. Nian, and Y. Gong, "Novel signal processing method for vital sign monitoring using FMCW radar," *Biomed. Signal Process. Control*, vol. 33, pp. 335–345, Mar. 2017.
- [24] H. Abdelnasser, K. A. Harras, and M. Youssef, "UbiBreathe: A ubiquitous non-invasive WiFi-based breathing estimator," in *Proc. 16th ACM Int. Symp. Mobile Ad Hoc Netw. Comput.*, Jun. 2015, pp. 277–286.
- [25] Y. Li et al., "DiverSense: Maximizing Wi-Fi sensing range leveraging signal diversity," *Proc. ACM Interact., Mobile, Wearable Ubiquitous Technol.*, vol. 6, no. 2, pp. 1–28, Jul. 2022.
- [26] F. Wang, F. Zhang, C. Wu, B. Wang, and K. J. R. Liu, "Respiration tracking for people counting and recognition," *IEEE Internet Things J.*, vol. 7, no. 6, pp. 5233–5245, Jun. 2020.
- [27] W. Li, R. J. Piechocki, K. Woodbridge, C. Tang, and K. Chetty, "Passive WiFi radar for human sensing using a stand-alone access point," *IEEE Trans. Geosci. Remote Sens.*, vol. 59, no. 3, pp. 1986–1998, Mar. 2021.
- [28] M.-C. Tang, F.-K. Wang, and T.-S. Horng, "Vital-sign detection based on a passive WiFi radar," in *IEEE MTT-S Int. Microw. Symp. Dig.*, Sep. 2015, pp. 74–75.
- [29] C. Li, V. M. Lubecke, O. Boric-Lubecke, and J. Lin, "A review on recent advances in Doppler radar sensors for noncontact healthcare monitoring," *IEEE Trans. Microw. Theory Techn.*, vol. 61, no. 5, pp. 2046–2060, May 2013.
- [30] K. Yamamoto, K. Toyoda, and T. Ohtsuki, "Doppler sensor-based blink duration estimation by analysis of eyelids closing and opening behavior on spectrogram," *IEEE Access*, vol. 7, pp. 42726–42734, 2019.
- [31] A. Ragman, V. M. Lubecke, O. Boric-Lubecke, J. H. Prins, and T. Sakamoto, "Doppler radar techniques for accurate respiration characterization and subject identification," *IEEE J. Emerg. Sel. Topics Circuits Syst.*, vol. 8, no. 2, pp. 350–359, Jun. 2018.
- [32] T. Sakamoto, P. J. Aubry, S. Okumura, H. Taki, T. Sato, and A. G. Yarovoy, "Noncontact measurement of the instantaneous heart rate in a multi-person scenario using X-band array radar and adaptive array processing," *IEEE J. Emerg. Sel. Topics Circuits Syst.*, vol. 8, no. 2, pp. 280–293, Jun. 2018.
- [33] M. Li and J. Lin, "Wavelet-transform-based data-length-variation technique for fast heart rate detection using 5.8-GHz CW Doppler radar," *IEEE Trans. Microw. Theory Techn.*, vol. 66, no. 1, pp. 568–576, Jan. 2018.
- [34] M. Le and B. Van Nguyen, "Multivariate correlation of higher harmonics for heart rate remote measurement using UWB impulse radar," *IEEE Sensors J.*, vol. 20, no. 4, pp. 1859–1866, Feb. 2020.
- [35] Y. Zhang, X. Li, R. Qi, Z. Qi, and H. Zhu, "Harmonic multiple loop detection (HMLD) algorithm for not-contact vital sign monitoring based on ultra-wideband (UWB) radar," *IEEE Access*, vol. 8, pp. 38786–38793, 2020.
- [36] C. Li et al., "A review on recent progress of portable short-range noncontact microwave radar systems," *IEEE Trans. Microw. Theory Techn.*, vol. 65, no. 5, pp. 1692–1706, May 2017.
- [37] J. Liu, Y. Li, C. Li, C. Gu, and J.-F. Mao, "Accurate measurement of human vital signs with linear FMCW radars under proximity stationary clutters," *IEEE Trans. Biomed. Circuits Syst.*, vol. 15, no. 6, pp. 1393–1404, Dec. 2021.
- [38] Y. Wang, W. Wang, M. Zhou, A. Ren, and Z. Tian, "Remote monitoring of human vital signs based on 77-GHz mm-Wave FMCW radar," *Sensors*, vol. 20, no. 10, p. 2999, May 2020.
- [39] L. Sun et al., "Remote measurement of human vital signs based on joint-range adaptive EEMD," *IEEE Access*, vol. 8, pp. 68514–68524, 2020.
- [40] F. Wang, X. Zeng, C. Wu, B. Wang, and K. J. R. Liu, "MmHRV: Contactless heart rate variability monitoring using millimeter-wave radio," *IEEE Internet Things J.*, vol. 8, no. 22, pp. 16623–16636, Nov. 2021.



Luyao Liu received the B.S. degree from the University of Science and Technology Beijing, Beijing, China, in 2018, where he is currently pursuing the Ph.D. degree.

His current research interests include radar signal processing, vital signs detection, machine learning, wireless sensor networks, and the Internet of Things.



Jie Zhang (Member, IEEE) received the Ph.D. degree from the University of Science and Technology Beijing, Beijing, China, in 2019.

He was a Visiting Research Fellow with the University of Leeds, Leeds, U.K., in 2018. From 2021 to 2022, he was an Associate Professor with the School of Automation and Electrical Engineering, University of Science and Technology Beijing. From 2019 to 2021, he was a Postdoctoral Research Fellow with Peking University, Beijing. He is currently a Marie Skłodowska Curie Research Fellow with the School of Electronic and Electronic Engineering, University of Leeds. His current research interests include pervasive computing, body sensor network, wireless sensor networks, and machine learning.

Dr. Zhang was a recipient of the Marie Skłodowska-Curie Actions Individual Fellowships (MSCA-IF), European Commission.



Ying Qu received the B.S. degree from the Tianjin University of Technology and Education, Tianjin, China, in 2018, and the M.S. degree from the University of Science and Technology Beijing, Beijing, China, in 2022.

She is currently with the Platform Capability Center, China Mobile Information Technology Company Ltd., Beijing. Her current research interests include signal processing, machine learning, data analysis.



Sen Zhang received the Ph.D. degree in electrical engineering from Nanyang Technological University, Singapore, in 2005.

She was a Postdoctoral Research Fellow with the National University of Singapore, Singapore, and a Lecturer In Charge with Singapore Polytechnic, Singapore. She is currently a Full Professor with the School of Automation and Electrical Engineering, University of Science and Technology Beijing, Beijing, China. Her current research interests include machine learning,

intelligent modeling and control of complex system, and autonomous vehicle.



Wendong Xiao (Senior Member, IEEE) received the B.S. and Ph.D. degrees from Northeastern University, Shenyang, China, in 1990 and 1995, respectively.

He held various academic and research positions with POSCO Technical Research Laboratories, Northeastern University, Pohang, South Korea; Nanyang Technological University, Singapore; and the Institute for Infocomm Research, Agency for Science, Technology and Research (A* STAR), Singapore. He is currently a Professor with the School of Automation and Electrical Engineering, University of Science and Technology Beijing, Beijing, China. His current research interests include intelligent wireless sensing, machine learning, big data processing, wireless localization and tracking, energy harvesting-based resource management, wireless sensor networks, and the Internet of Things.